Editors' Suggestion

Symmetry and planar chirality measured with a log-polar transformation in a transmission electron microscope

A.H. Tavabi,[1] P. Rosi,[2] R.B.G. Ravelli,[3] A. Gijsbers,[3] E. Rotunno,[2] T. Guner,[4] Y. Zhang,[3] A. Roncaglia,[5] L. Belsito,[5] G. Pozzi,[1,6] T. Denneulin,[1] G.C. Gazzadi,[2] M. Ghosh,[7] R. Nijland,[7] S. Frabboni,[6,2] P.J. Peters,[3] E. Karimi,[4] P. Tiemeijer,[7] R.E. Dunin-Borkowski,[1] and V. Grillo[2,*]

[1] *Ernst Ruska-Centre for Microscopy and Spectroscopy with Electrons, Forschungszentrum Jülich, 52425 Jülich, Germany*

[2] *Centro S3, CNR - Istituto di Nanoscienze, 41125 Modena, Italy*

[3] *Maastricht Multimodal Molecular Imaging Institute, Division of Nanoscopy, Maastricht University, Universiteitssingel 50, Maastricht 6229 ER, The Netherlands*

[4] *Department of Physics, University of Ottawa, Ottawa, Ontario K1N 6N5, Canada*

[5] *Istituto per la Microelettronica e Microsistemi (IMM) Consiglio Nazionale delle Ricerche (CNR), Via P. Gobetti 101, 40129 Bologna, Italy*

[6] *Dipartimento FIM, Universitá di Modena e Reggio Emilia, 41125 Modena, Italy*

[7] *Thermo Fisher Scientific, PO Box 80066, 5600 KA Eindhoven, The Netherlands*

(Received 22 March 2024; revised 5 May 2024; accepted 17 May 2024; published 31 July 2024)

Transmission electron microscopy can be described in terms of the measurement, in an appropriate quantum basis, of the quantum state of an electron after scattering through a sample. Recently developed methods for measuring the orbital angular momentum (OAM) of an electron beam using an OAM sorter can be used to reveal the *n*-fold symmetry of a sample. Here, we introduce and demonstrate a new composite planar chirality operator, which is based on rotation and scaling operators. By using synthetic electron holograms, we show that an electron OAM sorter can be used to determine the scaling symmetries and planar chiralities of relevant objects such as biomolecules, for which the technique could provide faster identification or help to achieve more detailed three-dimensional reconstructions by solving upside-down orientation ambiguities. A statistical analysis shows that, even for very low doses, this can be a solid indicator, even without the need for full imaging of the particle.

DOI: 10.1103/PhysRevApplied.22.014083

I. INTRODUCTION

Symmetries are fundamental quantities in nature, which provide insight into mechanisms of forces and conserved physical quantities [1–3]. As they are essential features in biology and life in general, the determination of the symmetry of an object can provide important information about physical or chemical processes [4,5]. On a basic level, an object possesses discrete translational, rotational, or parity symmetry when the Hamiltonian that describes its action is independent of the corresponding conjugate variables. This concept is known as the Noether theorem and the corresponding symmetry quantities are given by quantum Hermitian operators, such as linear momentum, orbital angular momentum, and the parity operator. When mirror symmetry is broken, a physical system becomes chiral [6]. Although chirality (which leads to phenomena such as birefringence and dichroism) can be defined, it is difficult to quantify "how chiral" an object is.

In a measurement, it is essential to be able to probe physical quantities in the most direct manner possible. The optimization of a measurement process, for example by increasing the number of quantities that can be measured, is a new trend in electron microscopy [7–12]. However, the fact that real-space representations still have a privileged role in quantum measurements lies at the foundation of quantum mechanics [13]. For example, measurements in an electron microscope are performed primarily in position (imaging), momentum (diffraction), and energy (electron energy-loss spectroscopy) spaces by making use of spatial dispersion through electron-optical elements. A recent addition to this list is the orbital angular momentum (OAM) sorter, which performs a wave transformation in log-polar coordinates and makes OAM decomposition visible on a detector [11,14,15]. For practical applications, an OAM sorter can be considered as an additional set of thin phase objects, which breaks the cylindrical symmetry

*Corresponding author: vincenzo.grillo@nano.cnr.it

of the microscope [16,17]. OAM sorters that are based on synthetic electron holograms [15], electrostatic phase elements [11], and structured magnetic elements have been demonstrated [18]. In Cartesian coordinates (x, y), an OAM sorter performs the conformal transformation via

$$(u_\rho, v_\theta) = \left(-s\log\left(\frac{\sqrt{x^2+y^2}}{b}\right), s\arctan(y/x)\right), \quad (1)$$

where s and b are scaling parameters, and $\log(\cdot)$ and $\arctan(\cdot)$ are logarithm and inverse tangent functions, respectively. After this transformation and ordinary diffraction, the quantity that is conjugate to v_θ, i.e., OAM, is sorted and observed on a detector [19–23]. If the electron propagates in the z-direction, then the OAM quantum mechanical operator is $L_z = -i\hbar(\partial/\partial v_\theta)$, where $\hbar$ is the reduced Planck constant. To complete the set of observables, one also needs to define the radial basis. Here, we define the logarithmic radial momentum $P_\rho = -i\hbar(\partial/\partial u_\rho)$, which is a conjugate of u_ρ. This radial operator should not be confused with the radial operator for Laguerre-Gaussian modes, which is a second-order derivative and depends on the azimuthal coordinate. The operator L_z generates an in-plane rotation $R = \exp(iL_z\delta v_\theta/\hbar)$. For an object that has m-fold symmetry, rotation by $\delta v_\theta = 2\pi/m$ leads to the same wave function, meaning that the spectrum of L_z is defined in multiples of m. In contrast, the quantity P_ρ has received much less attention. The transformation $T = \exp(iP_\rho\delta u_\rho/\hbar)$ produces a translation of the wave function in u_ρ space by an amount δu_ρ, where the quantity u_ρ is related to radial coordinates and a translation δu_ρ results in radial scaling of the wave function due to the logarithmic factor.

II. CONCEPT OF PLANAR CHIRALITY

We consider here a composition of the R and T symmetry operators in the form $R \otimes T$, in order to define a new planar symmetry that subtends an $O(1) \times U(1)$ group as a function of the two parameters δv_θ and δu_ρ. Waves that transform into themselves under this composite transformation have a logarithmic-spiral wave front with $\ell v_\theta + \kappa u_\rho =$ constant, where ℓ and κ are eigenvalues of L_z and P_ρ, respectively. Logarithmic spirals are self-similar to the scaling ℓ/κ and represent a specific form of planar chirality and ℓ-fold symmetry. The slope angle $\alpha = \arctan(\ell/\kappa)$ is the angle formed by the spiral with every concentric radius [24].

These considerations permit a new operator $\chi = L_z/P_\rho$, which we refer to as "in-plane chirality", to be defined. The variable χ measures how much a figure winds like a spiral, while its sign indicates the direction of the spiral (either clockwise or counterclockwise). This concept is related to the in-plane chirality of the object, albeit without considering its three-dimensional structure. It is a pseudoscalar

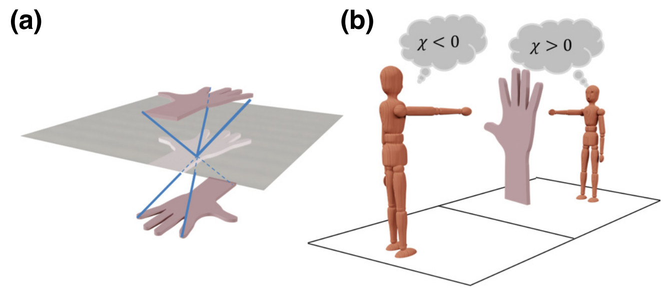

FIG. 1. (a) In-plane chirality, χ, does not change following an inversion through a point, but (b) it is a pseudoscalar quantity with odd parity on performing a mirror operation along z.

quantity since it is odd on performing a parity operation along z (the angular momentum operator L is a pseudovector, with L_z changing sign upon z inversion, while P_ρ does not). The z parity or mirror parity about a plane that contains z can be transformed into a single mirror symmetry upon log-polar transformation and subsequent diffraction. To be precise, a mirror symmetry in the OAM-P_ρ plane is transformed into a mirror symmetry about the $L_z = 0$ axis, while the direction of the symmetry plane is encoded in the phase (see Fig. 1). In this representation, it is intuitive to verify that an object that has at least one mirror symmetry plane is characterized by $\langle\chi\rangle = 0$.

Another interesting property of χ is that neither a rotation nor a center inversion of the form (x,y) –> $(-x, -y)$ have an effect on its amplitude spectrum. This point is relevant, as both transformations occur many times in an electron microscope. Conversely, a Fresnel propagation that introduces a parabolic phase in the propagating wave can alter the radial structure of the spiral. As a result, the quantity χ is only measured correctly when the image of an object is in-focus.

Chirality is often related to the optical activity of an object and to its differential response to an excitation such as light polarization [25]. Extrinsic chirality is related to the geometric form factor of the object. Here, we define the planar chirality of an object (or of a wave that has been scattered elastically by that object) independently of the detail of the probe, such as its wavelength. The quantity χ then represents a "universal" symmetry of the object and is scale-invariant.

If the effect of the object is primarily to alter the phase of the wave, as is typical in the imaging of proteins using electron microscopy, the value of χ is largely invariant to phase scaling by constant factors for both the radial and the angular parts. This relationship is not true for the OAM and P_ρ parts individually. Both of these properties are desirable for a quantity that aims to measure only a geometrical factor, regardless of the strength of coupling to a probe or its size scale.

It should be noted that χ is a self-adjoint operator in Hilbert space and that its spectrum, based on the full complex wave function, can be calculated exactly in OAM-P_ρ representation as $[\chi, L_z] = [\chi, P_\rho] = 0$. Conversely, it is useful to characterize an object by a single number. We can choose its expectation value $\langle \chi \rangle$, which can be calculated simply by its diagonal representation (see Supplemental Material [26]). Although the reduction of a shape to a single number means simplifying its potentially complex structure, it is a fast discriminator in the identification of experimental structures such as proteins, whose chiral structure is an essential feature.

For an ideal logarithmic spiral, χ is very much centered on a single value based on what is said above, and it could lead to different geometrical interpretations. For example, in spiral galaxies, which are approximatively logarithmic spirals, this parameter has been found to be correlated with the size of the central black hole [24]. Although there may not be a physical meaning in other structures, the average value of χ measures how much the wave projects onto each kind of spiral. A special case is that of an Archimedean spiral, where only one sign of the spiral prevails but χ has a full range of values. Practical problems in the calculations arise at all points with $\kappa = 0$, where the operator is not bounded. Since these components are not directly relevant to the chirality, we have adopted a regularized version of the operator.

In fact, the value of $\langle \chi \rangle$ is calculated according to the following formula:

$$\langle \chi \rangle = \frac{\sum_{k\neq 0,\ell\neq 0} (l/k) I_{\ell,k}}{\sum_{k\neq 0,\ell\neq 0} I_{\ell,k}},$$

where ℓ and κ are the OAM and P_ρ eigenvalues; $I_{\ell,k}$ is the corresponding intensity, as measured in the sorter OAM-P_ρ plane. The value of $\ell = 0$ is excluded because it is too dependent on the imaging conditions and radial cut-off details.

Figure 2 shows examples of planar chirality in nature. Here, we concentrate on the ESX-1 secretion-associated protein B (EspB) from *Mycobacterium tuberculosis* oriented along its main symmetry axis [27]. Considering that real-space imaging is the main mode of operation of an electron microscope, the most successful refinement of this idea would be its application in cryo-electron microscopy for the analysis of dose-sensitive proteins, which typically

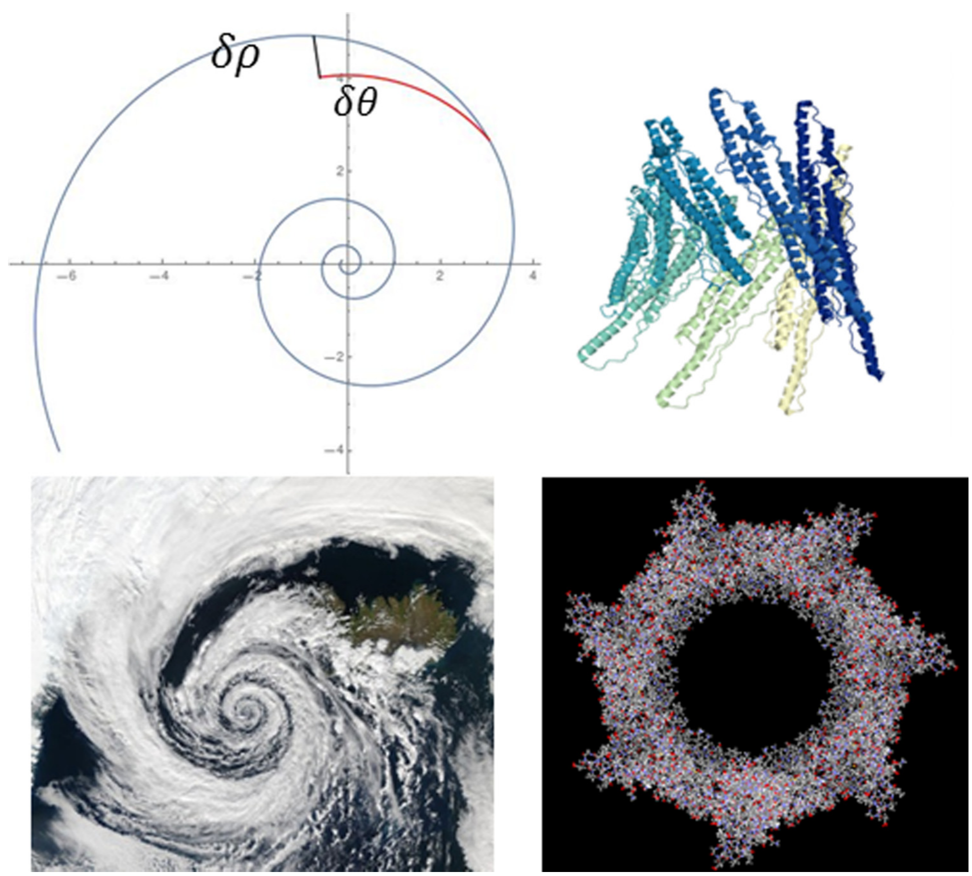

FIG. 2. (upper left) Abstract logarithmic spiral (separate azimuthal and radial translations are shown) and (lower left) its realization in nature in the form of a tornado. (upper and lower right) Structure of the ESX-1 secretion-associated protein B (EspB), the subject of the present study.

involves imaging multiple instances of the same object in random orientations embedded in a layer of vitreous ice [28,29]. Although this approach can be used for 3D reconstruction of dose-sensitive objects such as proteins, it is not yet applicable at the level of a single protein. However, direct identification of the symmetry of an individual protein would be of interest, both because ambiguity in an up-down orientation can result in ambiguity in 3D reconstruction and because it could enable the identification of specific characteristics of an object in a cell in the presence of other particles.

III. APPLICATIONS IN ELECTRON MICROSCOPY IMAGING

Transmission electron microscopy (TEM) images of proteins, formed with transmitted elastically scattered electrons, result in projections that do not inherently contain 3D information. However, in many cases, the projected structure is not mirror-symmetric about a plane, i.e., it has "planar chirality." Here, we consider a "virtual protein" produced by a computer-generated synthetic hologram [30]. The hologram reproduces the electron wave function that would have been formed by a real protein.

A synthetic hologram of a protein was fabricated by sculpting a thickness modulation in a thin membrane of SiN. This object is, to a good approximation, a phase object, i.e., an object whose primary effect is to modulate the phase of the electron wave that traverses through it. The action of the synthetic hologram is similar to that of a real protein, i.e., modulation of the phase of the incoming electron wave function. Although its lateral scale is 100 times larger than that of a real protein, it is decreased by positioning the hologram in the illumination condenser aperture of the electron microscope. In terms of the electron wave function, it is therefore equivalent to studying a virtual protein. Each synthetic hologram was prepared by using focused ion beam milling according to a computer-generated pattern. The SiN membranes were evaporated with Au, which was removed in a circular window in the hologram region. The diameter of the circle was 20 μm for the virtual protein and 40 μm for other holograms and spirals.

An electrostatic OAM sorter, which has been demonstrated for simpler structures [11], was placed in the projection part of the TEM. We used the FEI Titan "HOLO" microscope in Forschungszentrum Jülich at 300 kV. The hologram was inserted into the C2 diaphragm holder, while electrostatic sorter elements were inserted into the objective and selected area diffraction diaphragm holders (see Supplemental Material [26]). This situation mimics realistic operation with a protein illuminated by a plane wave. However, alignment of the optics is easier since the sample can sustain a higher electron dose. Working on a real protein would not add to the symmetry considerations presented here but would require additional experimental improvements, including fast artificial intelligence (AI) feedback control for the microscope and the sample for protein centering [31].

Figure 3 shows experimental results, which confirm that the sorter produces a log-polar conformal mapping of a wave function, which is then diffracted to form an OAM spectrum. Under ideal conditions, the OAM sorter produces a peak width that corresponds to an OAM value of 1 in units of $\hbar$. In calibration experiments, such as those shown in Fig. 3, we demonstrate here a near-ideal OAM resolution of $\Delta\ell = 1.1\,\hbar$ through an appropriate design of the electrodes and the use of AI for alignment of the system [32].

Figure 4 shows experiments performed using synthetic holograms of virtual proteins corresponding to two opposite orientations, as well as for an Archimedean spiral beam and a logarithmic-spiral beam. The first two columns describe the object, while the second image in particular

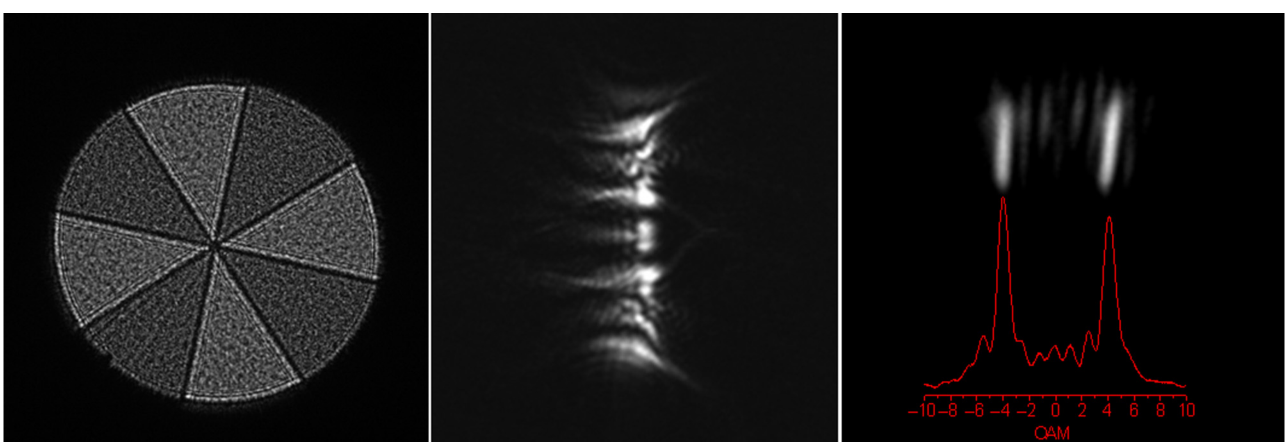

FIG. 3. OAM decomposition in a TEM for a nonchiral structure, demonstrating $1.1\hbar$ OAM resolution. (left) Original beam, (center) the same beam after conformal mapping, and (right) the corresponding OAM spectrum.

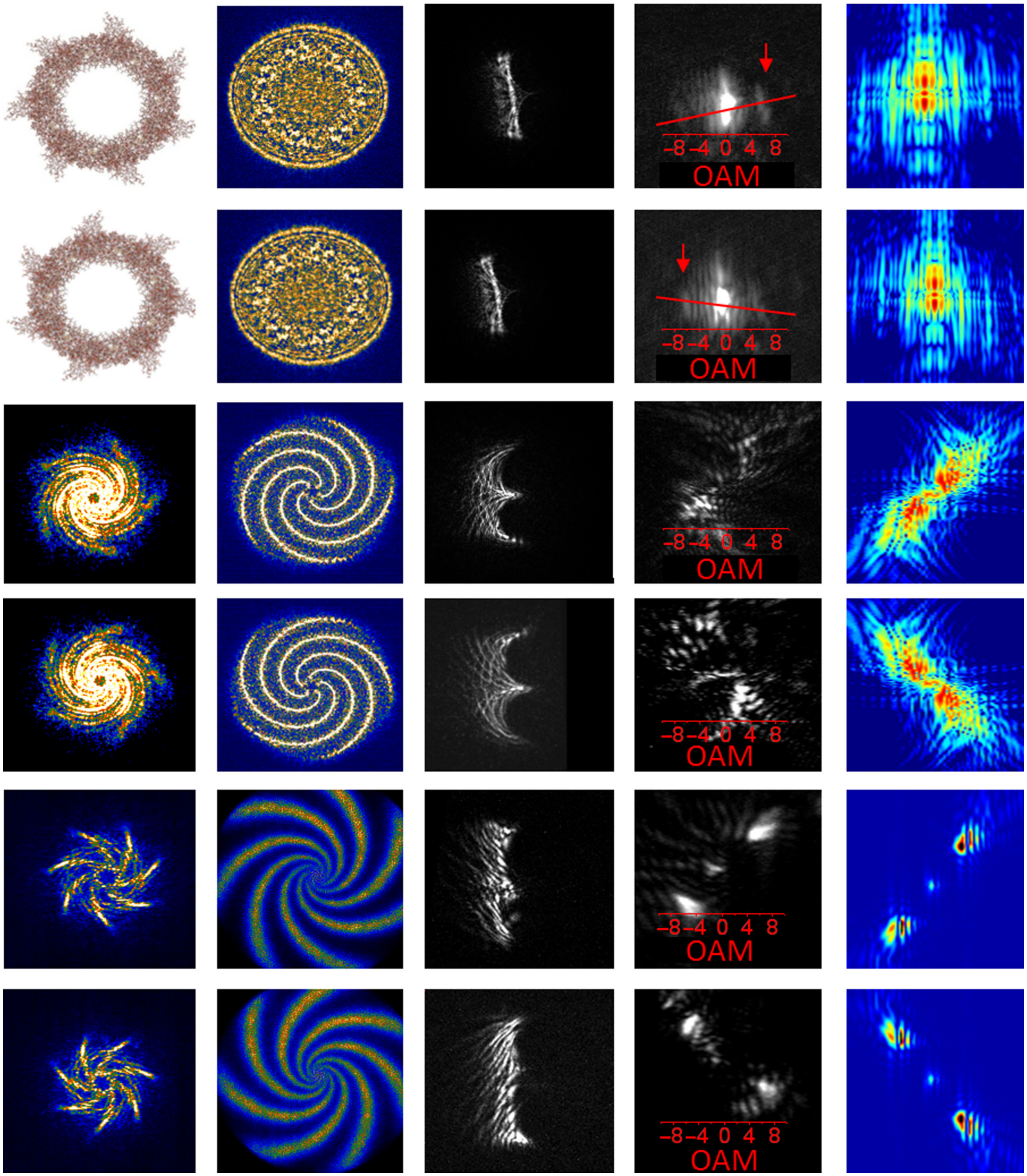

FIG. 4. OAM-P_ρ spectra from experimental analysis using (rows 1 and 2) an OAM sorter of a virtual protein, (rows 3 and 4) an Archimedean spiral beam, and (rows 5 and 6) a logarithmic-spiral beam. In each case, analyses are shown for both orientations. (first column) Real-space images recorded out-of-focus (or an atomistic model for the protein). (second column) In-focus images of the same object. (third column) Experimental log-polar representations obtained using an OAM sorter. (fourth column) OAM–P_ρ representations, i.e., the final outcomes of sorter diffraction. (fifth column) Corresponding simulation results.

is the slightly out-of-focus experimental image of the hologram. The other two experimental images display the log-polar transformed wave scattered by the object and the corresponding OAM-Pr spectrum. The latter is to be compared with the simulation (in color in the final column). The first two rows show a virtual EspB protein of

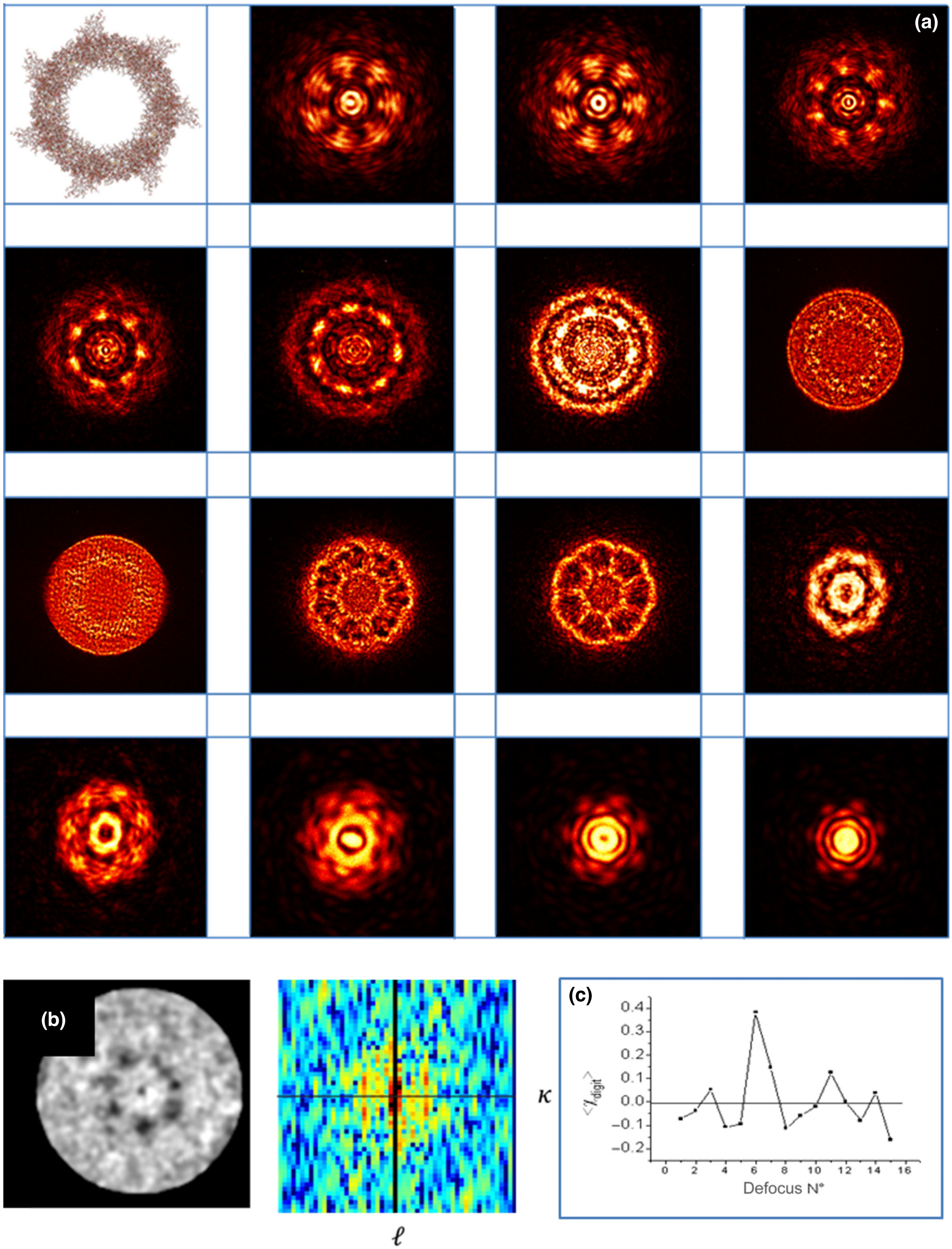

FIG. 5. (a) Experimental focal series of images of a virtual protein. (b) Experimental cryo-TEM image of a real protein and its digital analysis in log-polar coordinate and (c) estimated value of $\langle \chi \rangle$ based on the digital analysis of images in (a). The digital analysis of real images is typically not reliable.

Mycobacterium tuberculosis (also shown in Fig. 2), which has been thoroughly analyzed in a previous theoretical paper [10] as an example of a peculiar protein with a moderate planar chirality. The atomistic model in the main symmetric direction is shown in the first column.

The OAM sorter has a unique ability to evaluate planar chirality, which cannot be extracted by direct imaging. For example, the sevenfold symmetry of the virtual proteins shown in Fig. 4 is not evident in in-focus images. The fifth and seventh fold symmetry are also visible for the linear and logarithmic spiral but with a more peculiar structure in the Pr direction, which we describe below.

The standard imaging procedure for visualizing the phase of an object in an electron microscope involves altering the imaging plane and allowing for a small Fresnel propagation (out-of-focus imaging), which redistributes the intensity based on the local phase gradient but is incompatible with the analysis of chirality. An advantage of using the OAM sorter is that it works directly on the complex wave function, making the χ spectrum directly measurable as an intensity variation.

Although the sevenfold symmetry of the proteins can be determined from out-of-focus images, such images do not help to identify the clockwise or counterclockwise orientations of the "wings" of individual proteins. A full set of out-of-focus images is shown in Fig. 5(a).

By using the OAM sorter, we find that the values of spiral chirality defined above are $\langle\chi\rangle = +0.036$ and $\langle\chi\rangle = -0.028$ for the two proteins shown in Fig. 4. It is possible to distinguish between the two orientations based only on the sign of $\langle\chi\rangle$. For comparison, we obtained $\langle\chi\rangle = 0.005$ for the nonchiral structure shown in Fig. 3. This small deviation of $\langle\chi\rangle$ from zero is likely to be associated with noise in the measurements and imperfections in alignment, hologram fabrication, and the instruments. The absolute values of $\langle\chi\rangle$ for the two protein cases are small, as the asymmetry is located only in their external structures. The measured values are in good agreement with simulations, for which a range of $|\langle\chi\rangle| \in [0.020, 0.036]$ was obtained.

In the lower part of Fig. 4, Archimedean and logarithmic spirals (for an experimental focal series of the logarithmic spiral, see Supplemental Material [26]), for which the chirality is larger, are considered. These spirals are characterized by wave fronts of the form $\ell v_\theta + ku_\rho =$ constant and $\ell v_\theta + kr =$ constant, respectively. For the Archimedean spiral, the OAM-P_ρ spectrum contains two staggered speckles with left-right asymmetry. For the logarithmic spiral (lower two rows), the staggered points are similar to dots since such spirals are eigenstates of L_z and P_ρ operators (unlike standard vortex beams). For a clockwise spiral, the signs of OAM and P_ρ are opposite, i.e., they are either positive and negative or vice-versa. The two extreme situations for the spirals produce values of $\langle\chi\rangle = -0.157$ and $\langle\chi\rangle = 0.332$ for the Archimedean and $\langle\chi\rangle = 0.55$ and $\langle\chi\rangle = -0.48$ for the logarithmic cases. The absolute values are much larger than for the proteins, as expected for structures with much more chirality. We also notice that, for Archimedean spirals, χ increases toward the periphery of the vortex area.

With reference to Fig. 4, the values of $\langle\chi\rangle$ correspond to slope angles of -8° and 18°, respectively: the slope angle is not constant (resulting in blurring of the OAM–P_ρ spectrum). At the periphery of the hologram, its value is approximately 17°. For the case of a logarithmic spiral in the lower part of Fig. 4, the value of $\langle\chi\rangle$ are near single-valued and corresponds to angles of 29° and 25° close to the design value of 32° in the hologram. Although the success of the sorter method is evident, we can further show that direct out-of-focus imaging is unreliable for evaluating χ. For comparison, instead of the sorter analysis, we digitally analyzed out-of-focus images of experimental and virtual proteins (Fig. 5) and spirals. We found that the results completely depend on the electron-optical conditions and, in particular, the defocus. In a few cases, the apparent sign of the chirality was inverted [see Fig. 5(c)].

Finally, we analyzed the stability of the measurement of χ upon reduction of the dose. This has been accomplished using an experimental image at a high dose as a probability function and simulating the effect of a reduced dose via

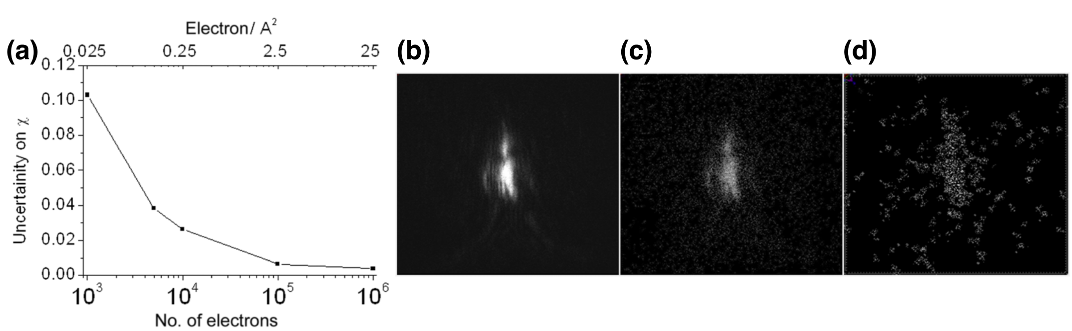

FIG. 6. (a) Standard deviation of the evaluation of $\langle\chi\rangle$ as a function of the number of electrons in an area of 20×20 nm for (b) a real high-dose experiment, as taken from Fig. 4 and simulated with a limited dose of (c) 2.5 $e\text{Å}^{-2}$ and (d) 0.25 $e\text{Å}^{-2}$. A very low dose, i.e., a few electrons, as in (d), is not sufficient to make a recognizable image but sufficient to extract the sign of $\langle\chi\rangle$.

a Monte Carlo algorithm. The double extraction approach permits us to randomly extract the electron according to a probability distribution given by the experimental high-dose image. Using this method, we were able to rigorously simulate the evaluation of $\langle \chi \rangle$ in controlled low-dose conditions.

We can describe, in particular, how the standard deviation of these evaluations and, therefore, the uncertainty decreases when increasing the dose. A plot of such standard deviation versus dose for the case of the protein in Fig. 4 is reported in Fig. 6. The plot indicates that even at a modest dose of 0.3 e/Å^2, which is very low for standard cryomicroscopy (in the range of 1–10 e/Å^2), the uncertainty on $\langle \chi \rangle$ is much smaller than the expectation value of 0.02, indicating that the sign of $\langle \chi \rangle$ is correctly evaluated in virtually all cases. This graph underlines the possibility of extracting a specific observable like $\langle \chi \rangle$ or at least its sign (namely the upside-down condition) even for dose-sensitive protein without a need to create a complete image of the object. We are reasonably below the dose-limited maximum information for this kind of sample, but this method shows a way to extract specific information without using the whole dose of electrons and causing possible damage, overcoming the need to acquire a full real-space image.

IV. CONCLUSIONS

In summary, we have shown that an OAM sorter can provide a new synthetic way to define and measure the planar chirality of an object with the characteristics of a fundamental symmetry and shape descriptor of an object. This quantity is important for cryo-electron microscopy of proteins, whose shape and symmetry are fundamental quantities.

The paper highlights that, for dose-sensitive materials, a unitary transformation of the electron wave allows us to extract specific properties of a sample without the need to perform full imaging. The quantitative definition of planar chirality, combined with the use of an OAM sorter, promises to improve coherent imaging in many scientific fields, including visible light optics and astronomy.

ACKNOWLEDGMENTS

This work received funding from the European Union's Horizon 2020 Research and Innovation Programme under Grants no. 766970 (QSORT), no. 964591 (SMARTelectrons), and no. 101035013 (MINOEN). T. G. and E. K. acknowledge the support from the Ontario Early Researcher Award (ERA) and the Canada Research Chairs (CRC) Program. This project received funding from the European Union's Horizon 2020 Research and Innovation Programme (Grant no. 823717, project "ESTEEM3").

This manuscript is dedicated to Prof. R.B.G. Ravelli, who had a big role in this paper and who passed away much too young.

[1] E. Noether, Invariante Variationsprobleme, Nachr. Ges. Wiss. Goettingen, Math. Kl. **1918**, 235 (1918).

[2] C. S. Wu, E. Ambler, R. W. Hayward, D. D. Hoppes, and R. P. Hudson, Experimental test of parity conservation in beta decay, Phys. Rev. **105**, 1413 (1957).

[3] D. E. Neuenschwander, *Emmy Noether's Wonderful Theorem* (JHU Press, Baltimore, 2017).

[4] J. R. Finnerty, The origins of axial patterning in the metazoa: how old is bilateral symmetry?, Int. J. Dev. Biol. **47**, 523 (2003).

[5] G. Holló, A new paradigm for animal symmetry, Interface Focus **5**, 20150032 (2015).

[6] W. T. B. Kelvin, *The Molecular Tactics of a Crystal* (Clarendon Press, Oxford, 1894).

[7] P. Schattschneider, S. Rubino, C. Hébert, J. Rusz, J. Kuneš, P. Novák, E. Carlino, M. Fabrizioli, G. Panaccione, and G. Rossi, Detection of magnetic circular dichroism using a transmission electron microscope, Nature **441**, 486 (2006).

[8] O. L. Krivanek, T. C. Lovejoy, N. Dellby, T. Aoki, R. W. Carpenter, P. Rez, E. Soignard, J. Zhu, P. E. Batson, M. J. Lagos, R. F. Egerton, and P. A. Crozier, Vibrational spectroscopy in the electron microscope, Nature **514**, 209 (2014).

[9] C. Schnell, Spatially resolved isotope labeling, Nat. Methods **16**, 287 (2019).

[10] F. Troiani, E. Rotunno, S. Frabboni, R. B. G. Ravelli, P. J. Peters, E. Karimi, and V. Grillo, Efficient molecule discrimination in electron microscopy through an optimized orbital angular momentum sorter, Phys. Rev. A **102**, 043510 (2020).

[11] A. H. Tavabi, P. Rosi, E. Rotunno, A. Roncaglia, L. Belsito, S. Frabboni, G. Pozzi, G. C. Gazzadi, P.-H. Lu, R. Nijland, M. Ghosh, P. Tiemeijer, E. Karimi, R. E. Dunin-Borkowski, and V. Grillo, Experimental demonstration of an electrostatic orbital angular momentum sorter for electron beams, Phys. Rev. Lett. **126**, 094802 (2021).

[12] X. Li, G. Haberfehlner, U. Hohenester, O. Stéphan, G. Kothleitner, and M. Kociak, Three-dimensional vectorial imaging of surface phonon polaritons, Science **371**, 1364 (2021).

[13] W. H. Zurek, Decoherence, einselection, and the quantum origins of the classical, Rev. Mod. Phys. **75**, 715 (2003).

[14] G. C. G. Berkhout, M. P. J. Lavery, J. Courtial, M. W. Beijersbergen, and M. J. Padgett, Efficient sorting of orbital angular momentum states of light, Phys. Rev. Lett. **105**, 153601 (2010).

[15] V. Grillo, A. H. Tavabi, F. Venturi, H. Larocque, R. Balboni, G. C. Gazzadi, S. Frabboni, P.-H. Lu, E. Mafakheri, F. Bouchard, R. E. Dunin-Borkowski, R. W. Boyd, M. P. J. Lavery, M. J. Padgett, and E. Karimi, Measuring the orbital angular momentum spectrum of an electron beam, Nat. Commun. **8**, 15536 (2017).

[16] B. J. McMorran, T. R. Harvey, and M. P. J. J. Lavery, Efficient sorting of free electron orbital angular momentum, New J. Phys. **19**, 023053 (2017).

[17] G. Pozzi, V. Grillo, P.-H. Lu, A. H. Tavabi, E. Karimi, and R. E. Dunin-Borkowski, Design of electrostatic phase elements for sorting the orbital angular momentum of electrons, Ultramicroscopy **208**, 112861 (2020).

[18] G. Pozzi, P. Rosi, A. H. Tavabi, E. Karimi, R. E. Dunin-Borkowski, and V. Grillo, A sorter for electrons based on magnetic elements, Ultramicroscopy **231**, 113287 (2021).

[19] J. Harris, V. Grillo, E. Mafakheri, G. C. Gazzadi, S. Frabboni, R. W. Boyd, and E. Karimi, Structured quantum waves, Nat. Phys. **11**, 629 (2015).

[20] K. Y. Y. Bliokh, I. P. P. Ivanov, G. Guzzinati, L. Clark, R. Van Boxem, A. Béché, R. Juchtmans, M. A. A. Alonso, P. Schattschneider, F. Nori, and J. Verbeeck, Theory and applications of free-electron vortex states, Phys. Rep. **690**, 1 (2017).

[21] S. M. Lloyd, M. Babiker, G. Thirunavukkarasu, and J. Yuan, Electron vortices: Beams with orbital angular momentum, Rev. Mod. Phys. **89**, 035004 (2017).

[22] B. J. McMorran, A. Agrawal, P. A. Ercius, V. Grillo, A. A. Herzing, T. R. Harvey, M. Linck, and J. S. Pierce, Origins and demonstrations of electrons with orbital angular momentum, Philos. Trans. R. Soc., A **375**, 20150434 (2017).

[23] H. Larocque, I. Kaminer, V. Grillo, G. Leuchs, M. J. Padgett, R. W. Boyd, M. Segev, and E. Karimi, 'Twisted' electrons, Contemp. Phys. **59**, 126 (2018).

[24] J. C. Berrier, B. L. Davis, D. Kennefick, J. D. Kennefick, M. S. Seigar, R. S. Barrows, M. Hartley, D. Shields, M. C. Bentz, and C. H. S. Lacy, Further evidence for a supermassive black hole mass-pitch angle relation, Astrophys. J. **769**, 132 (2013).

[25] S. Nechayev, J. S. Eismann, R. Alaee, E. Karimi, R. W. Boyd, and P. Banzer, Kelvin's chirality of optical beams, Phys. Rev. A **103**, L031501 (2021).

[26] See Supplemental Material at http://link.aps.org/supplemental/10.1103/PhysRevApplied.22.014083 for an experimental focal series for a logarithmic spiral generated by a SiN-based electron hologram. The series shows an evident change in the apparent planar chirality when traversing from the under- to over-focus. This again confirms that planar chirality cannot be derived from digital image analyses of out-of-focus images.

[27] M. Solomonson, D. Setiaputra, K. A. T. Makepeace, E. Lameignere, E. V. Petrotchenko, D. G. Conrady, J. R. Bergeron, M. Vuckovic, F. DiMaio, C. H. Borchers, C. K. Yip, and N. C. J. Strynadka, Structure of EspB from the ESX-1 type VII secretion system and insights into its export mechanism, Structure **23**, 571 (2015).

[28] R. Henderson, The potential and limitations of neutrons, electrons and X-rays for atomic resolution microscopy of unstained biological molecules, Q. Rev. Biophys. **28**, 171 (1995).

[29] R. Henderson, Avoiding the pitfalls of single particle cryo-electron microscopy: Einstein from noise, Proc. Natl. Acad. Sci. U. S. A. **110**, 18037 (2013).

[30] P. Rosi, F. Venturi, G. Medici, C. Menozzi, G. C. Gazzadi, E. Rotunno, S. Frabboni, R. Balboni, M. Rezaee, A. H. Tavabi, R. E. Dunin-Borkowski, E. Karimi, and V. Grillo, Theoretical and practical aspects of the design and production of synthetic holograms for transmission electron microscopy, J. Appl. Phys. **131**, 031101 (2022).

[31] P. Rosi, A. Clausen, D. Weber, A. H. Tavabi, S. Frabboni, P. Tiemeijer, R. E. Dunin-Borkowski, E. Rotunno, and V. Grillo, Automatic alignment of an orbital angular momentum sorter in a transmission electron microscope using a convolutional neural network, Microsc. Microanal. **29**, 408 (2023).

[32] E. Rotunno, A. H. Tavabi, P. Rosi, S. Frabboni, P. Tiemeijer, R. E. Dunin-Borkowski, and V. Grillo, Alignment of electron optical beam shaping elements using a convolutional neural network, Ultramicroscopy **228**, 113338 (2021).